



# Angle-dependent phononic dynamics for data-driven source localization

Weidi Wang, Amir Ashkan Mokhtari, Ankit Srivastava, and Alireza V. Amirkhizi 1,a)

#### **ABSTRACT:**

The source angle localization problem is studied based on scattering of elastic waves in two dimensions by a phononic array and the exceptional points of its band structure. Exceptional points are complex singularities of a parameterized eigen-spectrum, where two modes coalesce with identical mode shapes. These special points mark the qualitative transitions in the system behavior and have been proposed for sensing applications. The equi-frequency band structures are analyzed with focus on the angle-dependent modal behaviors. At the exceptional points and critical angles, the eigen-modes switch their energy characteristics and symmetry, leading to enhanced sensitivity as the scattering response of the medium is inherently angle-dependent. An artificial neural network is trained with randomly weighted and superposed eigen-modes to achieve deep learning of the angle-dependent dynamics. The trained algorithm can accurately classify the incident angle of an unknown scattering signal, with minimal sidelobe levels and suppressed main lobewidth. The neural network approach shows superior localization performance compared with standard delay-and-sum technique. The proposed application of the phononic array highlights the physical relevance of band topology and eigen-modes to a technological application, adds extra strength to the existing localization methods, and can be easily enhanced with the fast-growing data-driven techniques.

© 2023 Acoustical Society of America. https://doi.org/10.1121/10.0022325

(Received 26 May 2023; revised 21 September 2023; accepted 14 October 2023; published online 8 November 2023)

[Editor: Haiqiang Niu] Pages: 2904–2916

#### I. INTRODUCTION

Traditional angle-of-arrival (AoA) measurements rely on time-of-flight calculation or finding the maximum signal strength during antenna rotation, and their precision is limited especially when strong noise is present. Among the traditional phased array approaches, it has been shown that sensor arrays made of non-homogeneous material will provide extra information for localization calculations and effectively enhance the sensing directivity.2 Nonhomogeneous media, especially mechanical metamaterials (MMs) and phononic crystals (PCs), exhibit exotic properties associated with wave propagation due to the collective or local behavior of their micro-structures. These microstructured media can lead to unique features, such as wave attenuation, 3-7 topological insulation, 8 and angle-dependent dynamic properties, breeding new technological opportunities in controlling wave propagation. In phased array systems, the use of micro-structured media creates certain advantages<sup>10</sup> as they may allow for sub-wavelength response manipulation. Homogeneous medium as the sensor backbone material can only produce plain sinusoidal waves under oblique scattering. The wave phase is simply determined by Snell's law, and the wave amplitude remains constant along the interface. In contrast, periodic microstructured systems can generate richer features in their

responses not only through local amplitude and phase fields, but also due to the emergence of singularities in their band structure. This leads to enhanced angular sensitivity (against incorrect estimation from adjacent angles) for measurement along the scattering interface. The objective of this work is to leverage the micro-structural features in phononic/metamaterial eigen-modes and exploit their angle-sensitive nature for the purpose of AoA estimation.

An emerging field of study in phononic and metamaterial research is the topic of exceptional points (EPs). EPs<sup>11</sup> are spectral singularities, initially identified in quantum mechanics studies. An EP is a point in a parametric non-Hermitian system, where two or more eigen-modes coalesce with identical eigenvalues and eigen-modes. The unique topology of the band structure near the EP degeneracy has been shown to lead to improved sensitivity. 12 In mechanical systems, abrupt changes in the eigen-modes are identified near the EPs. 13,14 Therefore, it is proposed to develop sensing devices in various physical setups 15-17 using EPs. However, the EP appears in the literature mostly as a mathematical and abstract concept because accessing these EPs is physically difficult [e.g., requires gain units in parity-time (PT) symmetric medium<sup>13,18</sup>]. This work studies the eigenmode and EP behaviors in phononic crystal systems and explores their potential applications, such as source localization in sonar systems. The research questions to be answered are (1) how to access the EP(s) in the wave scattering problem, (2) how an EP affects the scattering behavior with

<sup>&</sup>lt;sup>1</sup>Department of Mechanical Engineering, University of Massachusetts, Lowell, Lowell, Massachusetts 01854, USA

<sup>&</sup>lt;sup>2</sup>Department of Mechanical, Materials, and Aerospace Engineering, Illinois Institute of Technology, Chicago, Illinois 60616, USA

a)Email: alireza\_amirkhizi@uml.edu

changing angles of incidence, and (3) how to leverage the eigen-mode knowledge to develop robust sensing approaches.

The problem is attacked using a two-dimensional (2D) stress wave oblique scattering setup. A periodic array of phononic crystals is used as the sensor medium to collect signals of oblique stress waves incident from a homogeneous medium (see Fig. 1). The wavevector k in this oblique scattering problem includes two components:  $k_1$  parallel to the interface and  $k_2$  normal to the interface. The parameter  $k_1$  is related to the incident angles through Snell's law in the incident (homogeneous) domain. For linear elastodynamic problems without loss or gain mechanism, the governing equations are self-adjoint (Hermitian) with real-valued eigenfrequencies, which prohibits the existence of EPs. An alternative form of governing equations may be arrived at by solving for the eigen-wavevector component  $k_2(\omega, k_1)$ (Ref. 19) and is useful for finding the oblique scattering wave field when a wave is incident at the interface between two domains. 20 In such problems, the frequency  $\omega$  and wavevector component  $k_1$  are prescribed as real values based on the incident wave, and one solves for the complex  $k_2$  wavevector normal to the interface. It has been shown that this modified eigen-problem representation allows for accessing EPs with real-valued frequencies and wavevectors. This addresses the first research question.

The second question can be answered by analyzing the  $k_2(\omega, k_1)$  band structure and associated eigen-modes, as this representation provides the critical opportunity to express the reflected/transmitted scattering signals at the interface as a weighted sum of the eigen-modes. Two types of branch points are identified in this representation of the phononic band structure. Both types of branch points have anglesensitive natures and are the spectral boundaries between propagating modes and evanescent ones. The first type of branch point is related to the critical angles<sup>21</sup> (CAs), where one wavevector solution transitions from purely real to imaginary (or vice versa). The modes associated with the CAs have zero wavevector component normal to the boundary, which leads to total internal reflection.<sup>22</sup> The second type of branch point is identified as EPs where two modes share identical eigenfunctions. In a setup<sup>23</sup> similar to this work, unusual energy transport is found at the EPs. However, the use of EPs for sensing applications has not been studied in elastodynamic problems. In the present study, spontaneous symmetry breaking is found at the CAs and the EPs, where the modes transition between propagating bulk modes, which exhibit symmetric eigenfunctions, and zero-energy edge modes, having asymmetric eigenfunctions. Since the eigen-modes may be used as basis functions of the scattered wave, the analysis can be effectively conducted within the subspace spanned by the dominant modes. Such a subspace inherently has angle-dependent features of the eigen-modes. This motivates the use of the spanned subspace to improve the estimation of angle of arrival in response to the third research question.

The presence of the modal branch points, hence, will lead to stronger qualitative sensitivity on the angle. To leverage the knowledge of the rich modal features in sensing applications, a deep neural network (NN) is constructed to relate the modal features with the incident angle, thus, providing an effective tool for estimating the bearing angle. Modern data-driven methods have the potential to learn hidden mechanisms and approximate complicated input-output relations. Niu et al. 24,25 showed the promising potential of using three machine learning (ML) methods for estimating acoustic source ranges. Ozanich et al.<sup>26</sup> presented a thorough study on AoA estimation with linear supervised learning methods and showed that the ML methods lead to improved resolution over the conventional approach. While previous works have primarily focused on ML methods with traditional array setups, we extend the existing methods by investigating the utilization of micro-structural features for their potential additional sensitivity, harnessing the potential of eigen-mode physics, to improve the accuracy of AoA estimation. In the present study, the source localization application is approached as a supervised multi-label classification problem. The eigen-mode behaviors are first studied in Sec. II. In Sec. III, the eigen-modes associated with each angle are randomly weighted and summed to serve as the training input. With a large enough set of these training samples, the NN can learn and identify the angle-dependent features of the subspace spanned by the eigen-modes. Although the scattering signal is unknown to the trained NN, the abstract features of its underlying subspace associated with each angle have been fed into the NN. Therefore, the NN can accurately identify the incident angle of an unknown scattering signal. This approach is shown to have significant improvements compared with conventional localization algorithms, such as delay-and-sum (DAS), in terms of the main lobewidth and the sidelobe levels. In addition, the signal sensitivity comparison between phononic crystals and

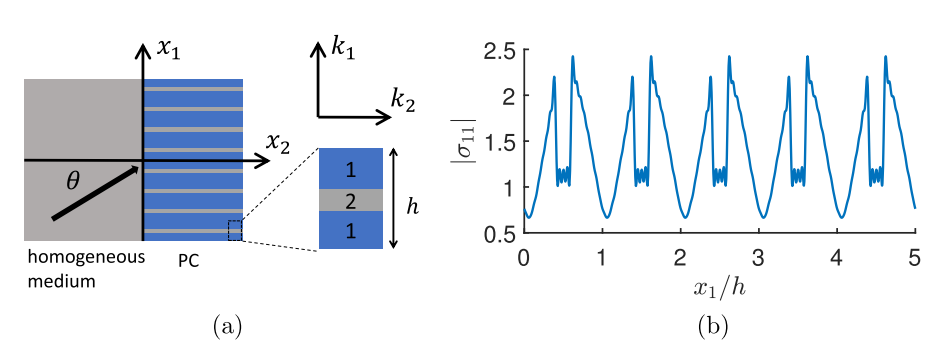


FIG. 1. (Color online) (a) The setup of 2D stress wave scattering at the interface between a homogeneous medium and an array of phononic crystals. Left and right domains are semi-infinite. The incident oblique wave is denoted by the arrow with an angle  $\theta$  measured from the normal to the interface. (b) Example response amplitude from 77° incidence along the interface over five unit cells.

homogeneous media is presented to highlight the importance of micro-structural features.

#### II. BAND STRUCTURE AND EIGEN-MODE ANALYSIS

In this section, we first briefly revisit the  $k_2(k_1,\omega)$  eigenvalue formulation for the oblique scattering problem. Then we discuss the band structure topology and the eigenmode properties of a typical and simple phononic array, with particular focus on the symmetry breaking at the branch points.

The studied scattering problem is formulated similarly as in a previous work<sup>27</sup> except for the different frequency range and unit cell size used here. An in-plane stress wave is incident from a semi-infinite domain of homogeneous medium to a phononic array with an incident angle  $\theta$  normal to the interface, as illustrated in Fig. 1.

For the plane wave propagating problem in the two semi-infinite domains, it is advantageous to know a priori the band structure that characterizes the dynamics of each domain. The common representation of a band structure presents the eigenfrequency  $f = \omega/2\pi$  as functions of wavevector  $(k_1, k_2)$  within the irreducible Brillouin zone. Figure 2(a) shows the first two eigen-surfaces of the studied phononic unit cell. Of particular interest for the scattering problem are the solutions at the constant operating frequency, in this case, 1800 Hz. The intersections of the eigenfrequency surfaces with a constant frequency plane (indicated by gray shading) are the eigen-modes of propagating waves. Figure 2(b) shows the equi-frequency contours for frequencies from 1740 to 1920 Hz. Certain branches are found to form collapsed modes. For example, the red circular markers in Fig. 2(b) denote the coalesced modes with merging  $k_2$  values for the same  $k_1$ . These branch points are the boundaries of the solutions with real  $k_2$ . Therefore, the identification of their locations is important for understanding the scattering physics. It must be noted that the eigen-modes obtained through this eigenfrequency analysis only partially constitute the scattering solution, because (1) the evanescent modes with complex  $k_2$  values are absent, and (2) one also needs to consider higher order modes not inside the irreducible Brillouin zone and select the correct branches that carry energy in the correct  $k_2$  direction (away from the interface). Therefore, an alternative formulation that can provide the full set of  $k_2(\omega, k_1)$  solutions is needed.

The displacement and stress solutions in one unit cell have the form

$$u_i(x_1) = \bar{u}_i(x_1) \exp\left[i(k_1x_1 + k_2x_2 - \omega t)\right]$$
 (1)

and

$$\sigma_{ij}(x_1) = \bar{\sigma}_{ij}(x_1) \exp[i(k_1x_1 + k_2x_2 - \omega t)].$$
 (2)

Here,  $u_i$  is the displacement components,  $\sigma_{ij}$  is the ij component of stress tensor,  $k_2$  is the wavevector component normal to the interface, and  $\omega$  is the angular frequency. The barred quantities are the periodic parts within one unit cell. The wavevector component  $k_1$  is parallel to the interface and is hence related to the incident angle  $\theta$  through Snell's law,

$$k_{in}\sin\theta = k_1,\tag{3}$$

where  $k_{in} = \omega/c_{\phi}$  is the wavevector of the incident wave, and  $c_{\phi}$  is the incident wave speed in the homogeneous medium (longitudinal or shear). The continuity at the interface between two domains requires that for each angle of incidence, a real-valued  $k_1h \mod 2\pi$  is prescribed in the non-Hermitian eigenvalue problem, from which an infinite number of  $k_2$  eigenvalues can be found. With  $\gamma = [k_1, 0]$  and  $\mathbf{n} = [0, k_2]$ , the  $k_2(\omega, k_1)$  eigenvalue problem is formulated as

$$\mathbf{A}\bar{\phi} = k_2 \mathbf{B}\bar{\phi},\tag{4}$$

where the mode shape is described by  $\bar{\phi} = [\bar{\mathbf{u}}, \bar{\boldsymbol{\sigma}}]^{\top}$ , and

$$\mathbf{A} = \begin{pmatrix} \omega^{2} \rho() & \nabla \cdot () - i() \cdot \gamma \\ -\mathbf{C} : \nabla() + i\mathbf{C} : () \otimes \gamma & \mathbf{I} \end{pmatrix}, \quad (5)$$

$$\mathbf{B} = \begin{pmatrix} \mathbf{0} & \mathbf{i}() \cdot \mathbf{n} \\ -\mathbf{i}\mathbf{C} : () \otimes \mathbf{n} & \mathbf{0} \end{pmatrix}. \tag{6}$$

The bold symbols  $\{\bar{\mathbf{u}}, \bar{\boldsymbol{\sigma}}\}$  represent quantities as vectors, which include the in-plane components,  $\mathbf{C}$  is the elasticity modulus, and  $\rho$  is the density. The details of this eigenvalue problem can be found in Ref. 19. An alternative method for computing complex  $k_2$  values is to use an

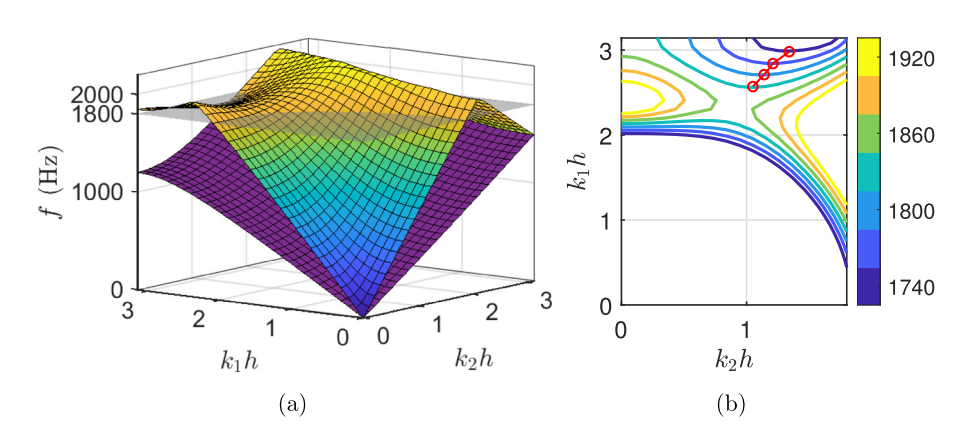


FIG. 2. (Color online) Eigenfrequency band structure of the phononic unit cell (a) and the equi-frequency contours at different frequencies (b).

optimization approach, which is briefly mentioned in Ref. 28. In the solutions considered here, the frequency  $f = \omega/2\pi = 1.8 \, \text{kHz}$  is constant, and the wavevector component  $k_2$  values are solved as complex eigenvalues for the varying parameter  $k_1$ .

# A. Scattering band structures

The  $k_2(\omega, k_1)$  band structures of the homogeneous domain and the phononic domain are partially shown in Figs. 3(a) and 3(b), respectively. The complete spectra will have symmetry with respect to  $k_2 = 0$ . Only the modes that have physical meanings in the scattering problem are considered and shown here. Therefore, the phononic band solved here partially overlaps with the previously shown equi-frequency contour Fig. 2(b). A physically feasible eigen-mode of the homogeneous medium, representing the reflected wave solution, must (1) have non-positive energy flux vector component  $F_2$  and (2) have  $\Im k_2 \leq 0$ . Similarly, to represent a transmitted wave solution, a phononic eigenmode must (1) have non-negative energy flux vector component  $F_2$  and (2) have  $\Im k_2 \ge 0$ . The modes violating these requirements are not taken into consideration. The (1) requirements ensure that the reflected/transmitted waves transfer energy away from the interface. The (2) requirements prevent infinitely large amplitudes at  $x_2 = \pm \infty$ , given the solution forms Eqs. (1) and (2). For each domain, only several modes with lowest  $|\Im k_2|$  values are shown in the band structure. Each of the solved eigen-modes represents a wave whose spatial features in  $x_2$  are determined by its  $k_2$ wavevector. A mode that has a real  $k_2$  eigenvalue will propagate and carry energy in  $x_2$  direction. A mode with complex eigenvalue, on the other hand, only allows the wave to propagate along the interface and is evanescent in  $x_2$  direction. As the incident angle varies, certain modes can transition from propagating to evanescent and vice versa.

In the reflected solutions [Fig. 3(a)], mode 1 represents the shear vertical wave reflected from the interface and is a propagating mode for any incident angle  $\theta$ . The reflected mode 2 contains three branches and two CAs (CA1 and CA2) in between them. The real-valued branch from  $0^{\circ}$  to  $30.3^{\circ}$  is the longitudinal wave that can propagate in the bulk of the homogeneous medium. The purely imaginary branch from  $30.3^{\circ}$  to  $47.2^{\circ}$  is the surface mode that does not allow

energy flux along  $x_2$ . The third branch, corresponding to reflection angles from 47.2° to 89°, is the shear mode of the second Brillouin zone and has real  $k_2$  eigenvalues. The two CAs at 30.3° and 47.2° are boundaries between propagating and evanescent modes.

The band structure of transmitted waves in Fig. 3(b) has more spectral features due to the micro-structure of the layered medium. Mode 1 has purely real eigenvalues and is, thus, a propagating mode. Modes 2 and 3 coalesce at the EP, associated with the exceptional angle (EA:  $35.1^{\circ}$ ). Two CAs can be found in modes 2 and 3 (CA3,  $48.8^{\circ}$ ; CA4,  $78.4^{\circ}$ ). The existence of these branch points is not particular to the selected  $1800\,\text{Hz}$  frequency and is dependent on the band topology. Their corresponding  $k_1$  values vary with frequency, as can be seen in Fig. 2. It is found that the EA exists from 0 to  $1855\,\text{Hz}$ . The CA CA3 appears in the frequency range of  $1720{-}1855\,\text{Hz}$ , as does its symmetric counterpart CA4 in the second Brillouin zone.

These special angles are associated with the emergence or annihilation of energy-carrying branches. At the EP, the eigenvalues and eigenfunctions of the two modes (2 and 3) will be identical. From 0° incidence to 35.1° incidence, mode 2 has purely imaginary eigenvalues, while mode 3 has real eigenvalues. At the EP, the eigenvalues of the two modes are identical and close to zero. From EA (35.1°) to CA3 (48.8°), the eigenvalues of modes 2 and 3 share the same imaginary parts, while their real parts are negatives of each other. Modes 2 and 3 become propagating from CA3 to CA4 (78.4°) and have distinct real-valued eigenvalues. For angles from CA4 to 89°, modes 2 and 3 again possess complex-valued eigenvalues. For the entire angle range, modes 4 and 5 share the same  $\Im k_2 h$  [the dotted lines overlapped as the right-most curve in Fig. 3(b)]. Their real parts of  $k_2h$  are negatives of each other. Due to their complexvalued  $k_2$  eigenvalues, modes 4 and 5 are evanescent modes.

# B. Modal symmetry and energy flux

In the oblique scattering problem, the reflected/transmitted waves in two domains are composed of all the eigensolutions at the corresponding  $k_1h$  value of the incident wave. Therefore, the physical properties of scattering signals are affected by not only the  $k_2$  eigenvalues but also the mode shapes. The displacement mode shapes of the periodic

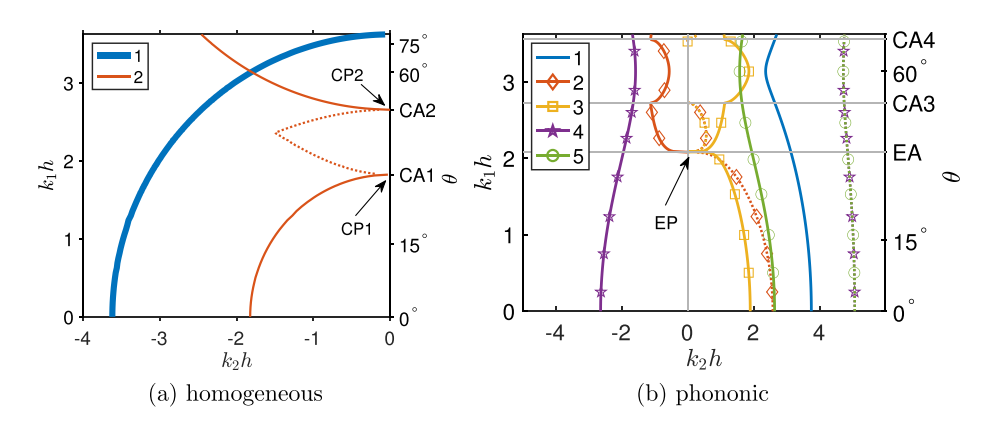


FIG. 3. (Color online) Wavevector band structures of the reflected waves in the homogeneous domain (a) and the transmitted waves in the phononic domain (b) at  $1.8 \, \text{kHz}$ . The  $k_2 h$  values have real (solid) and imaginary (dotted) components. Only the first several important modes are shown.

2907

cell along the interface are analytically obtained from the eigenvectors in Eq. (4). The normalized amplitudes and complex arguments are shown for different incident angles, in Figs. 4 and 5, respectively. The presented four mode shapes are the displacement mode shapes corresponding to the first four modes in Fig. 3(b). The unit cell inversion center is set to be  $x_1 = 0$ . For each mode and each angle  $\theta$ , the complex displacements are normalized so that  $||[\bar{\mathbf{u}}_1^{(m)}, \bar{\mathbf{u}}_2^{(m)}]^\top|| = 1$ , and  $\Im[\bar{u}_1^{(m)}(x_1 = -h/2)] = 0$ , where the superscript denotes the mth mode, and the bold symbol denotes the vector form of a quantity along  $x_1$ . For modes 2 and 3, three vertical dashed lines are plotted at EA (35.1°), CA3 (48.8°), and CA4 (78.4°).

It can be seen that, for modes 1 and 4, the displacements  $\bar{\mathbf{u}}_{1,2}^{(1,4)}$  are relatively smooth and continuous with respect to the variation in angle, as their eigenvalues  $k_2^{(1,4)}(\theta)$  do not undergo branch crossing or coalescence. Mode 5 is not shown here but has a similar nature to mode 4. For modes 2 and 3, clear transitions in  $\bar{\mathbf{u}}_{1,2}^{(2,3)}$  can be found at the three special angles marked by the dashed lines, both in their amplitudes and arguments. Spectral transitions in the  $k_2$  eigenvalues, therefore, lead to drastic changes in the associated wave mode shapes. Although only the displacement components of the mode shapes are shown, the stress components also share similar transitions at these angles.

The mode shape patterns change their symmetries as well when the incident angle sweeps through the EA and CAs. It turns out that the EP and CAs have underlying relations with spontaneous symmetry breaking. The phononic unit cell shown in Fig. 1 possesses parity symmetry with

respect to its inversion center  $x_1 = 0$ . The governing equation is invariant if the phononic parity is reversed. Along a line of constant  $x_2$ , the displacement wave associated with a certain mode with a positive  $k_1$  value is

$$u_{1,2}^{+}(x_1,t) = |\bar{u}_{1,2}(x_1)| \exp\left(i(\bar{\varphi}_{1,2}(x_1) + \bar{\varphi}_0 + k_1 x_1 - \omega t)\right),\tag{7}$$

where the superscript + denotes a wave with positive  $k_1$  value,  $\bar{\varphi}(x_1)$  is the complex argument of  $\bar{u}_{1,2}(x_1)$ , and the  $k_2$  dependence is omitted since  $x_2$  is constant here. Here,  $\bar{\varphi}_0$  is an arbitrary real phase applied to the eigen-mode displacement field and should be consistent for both  $u_1$  and  $u_2$ . Similarly, for the same wave at  $-x_1$ , we have

$$u_{1,2}^{+}(-x_1,t) = |\bar{u}_{1,2}(-x_1)| \exp(i(\bar{\varphi}_{1,2}(-x_1) + \bar{\varphi}_0 - k_1x_1 - \omega t)).$$
(8)

Now we consider a wave of the same mode propagating in a reversed direction, the wavevector component  $k_1$  becomes negative, and the displacement at  $-x_1$  is

$$u_{1,2}^{-}(-x_1,t) = |\bar{u}_{1,2}(-x_1)| \exp\left(i(-\bar{\varphi}_{1,2}(-x_1) - \bar{\varphi}_0 + k_1x_1 - \omega t\right)\right). \tag{9}$$

Equation (9) is in such a form because  $\Re[u_{1,2}^+(t)] = \Re[u_{1,2}^-(-t)]$  must be satisfied. Given the parity symmetry of the unit cell, it is expected that

$$u_{1,2}^{+}(x_1,t) = u_{1,2}^{-}(-x_1,t)$$
(10)

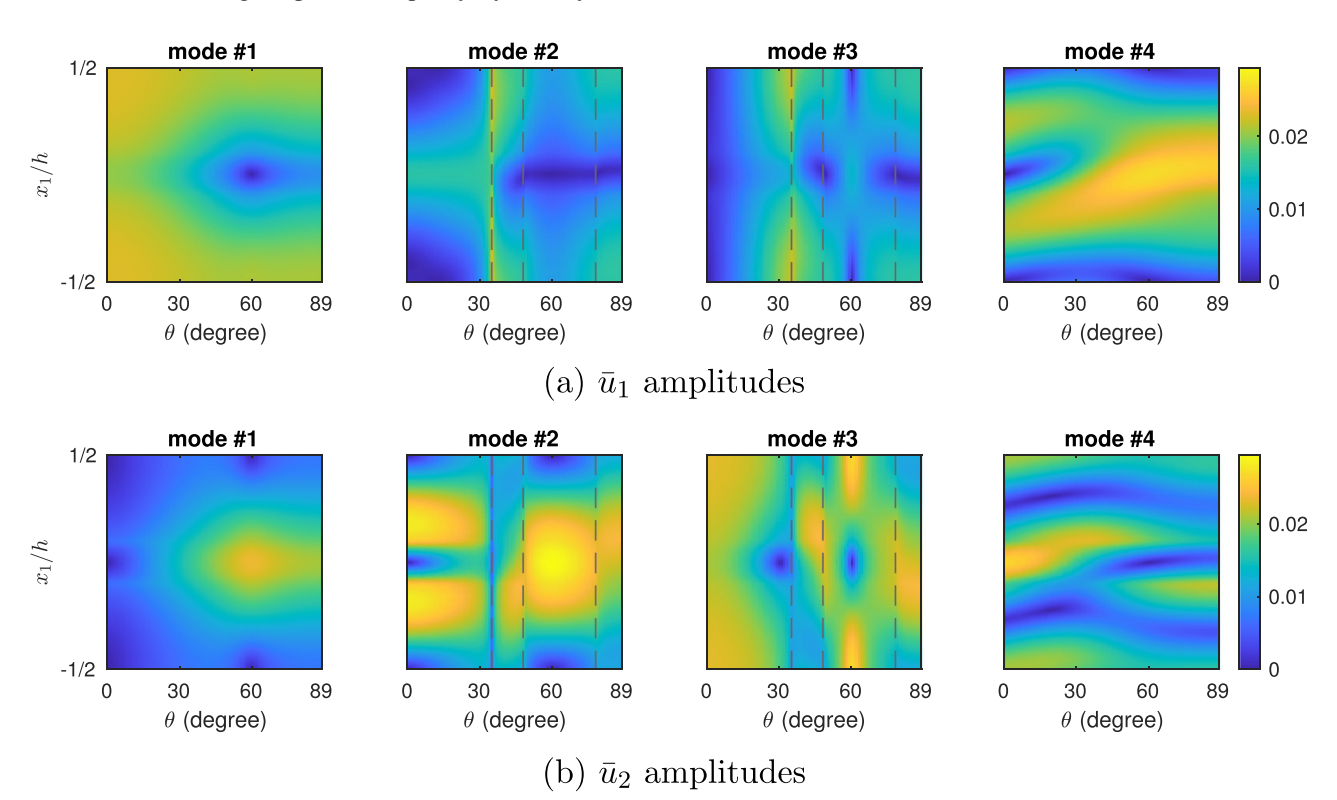


FIG. 4. (Color online) Normalized mode shapes evaluated along the  $x_1$  interface as functions of incident angle  $\theta$ : (a) amplitudes of  $\bar{u}_1$ ; (b) amplitudes of  $\bar{u}_2$ . The angles associated with EP and CAs are marked by the vertical dashed lines in the mode 2 and 3 graphs.

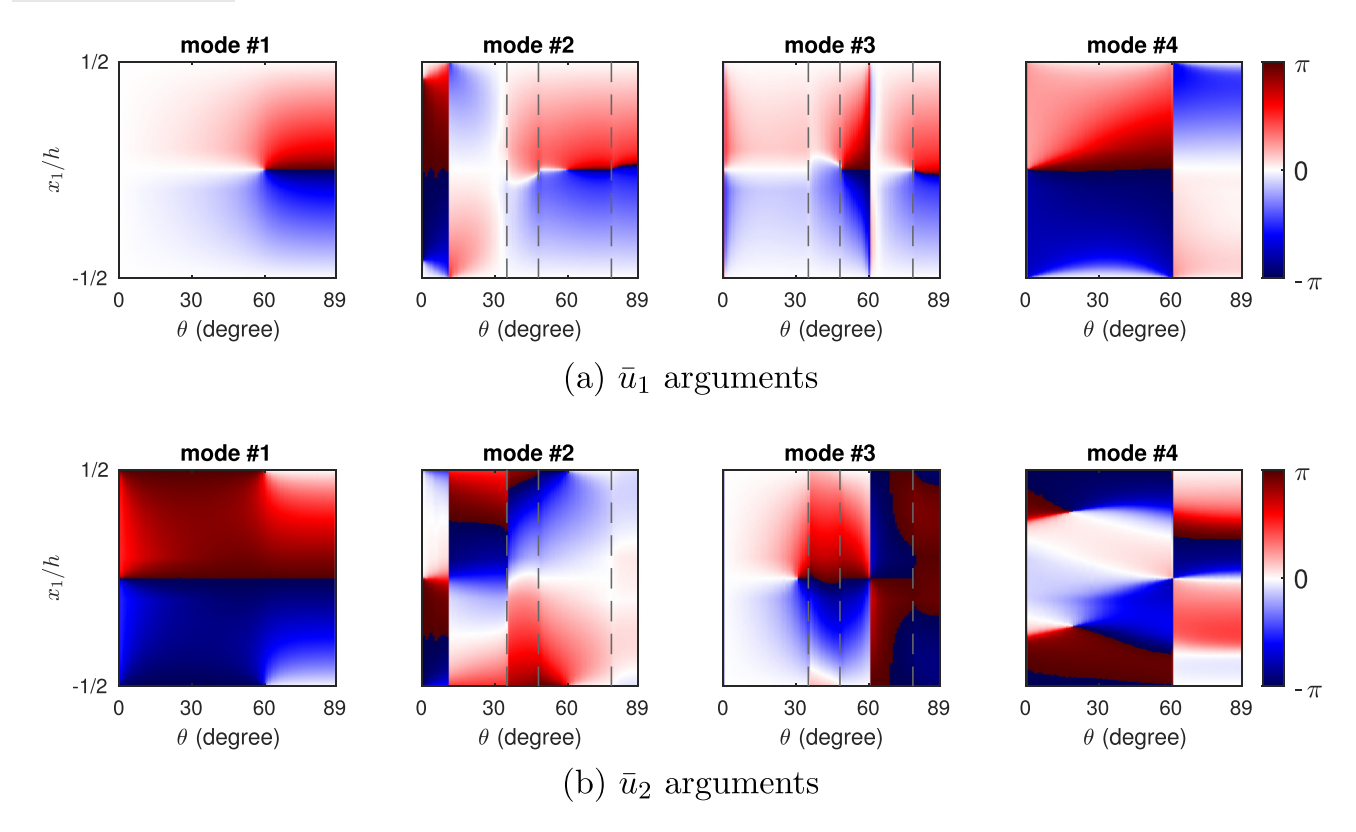


FIG. 5. (Color online) Normalized mode shapes evaluated along the  $x_1$  interface as functions of incident angle  $\theta$ : complex arguments of (a)  $\bar{u}_1$  and (b)  $\bar{u}_2$ . The angles associated with EP and CAs are marked by the vertical dashed lines in the mode 2 and 3 graphs.

for a mode in the symmetry-unbroken phase. Equation (10) reveals that a symmetry-unbroken mode shape (for the *m*th mode) must satisfy

$$\begin{aligned} |\bar{u}_{1,2}^{(m)}(x_1)| &= |\bar{u}_{1,2}^{(m)}(-x_1)|,\\ \bar{\varphi}_{1,2}^{(m)}(x_1) &+ \bar{\varphi}_{1,2}^{(m)}(-x_1) &= -2\bar{\varphi}_0^{(m)} = \text{const.} \end{aligned}$$
(11)

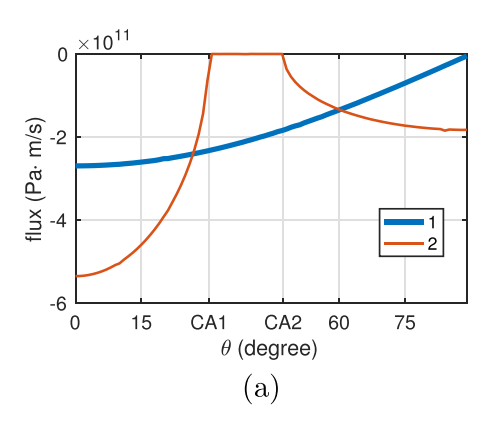
Since the displacement vector is normalized in such a way that  $\bar{\varphi}_1^{(m)}(-h/2)=0$ , we have  $\bar{\varphi}_0^{(m)}=0$ . In other words, the amplitudes must be symmetric with respect to the cell inversion center, while the arguments must be anti-symmetric. It is shown in Figs. 4 and 5 that the symmetry-unbroken conditions in Eq. (11) are satisfied for branches with purely real  $k_2$  eigenvalues, i.e., mode 1 from  $0^{\circ}$  to  $89^{\circ}$ , mode 2 from  $CA3=48.8^{\circ}$  to  $CA4=78.4^{\circ}$ , and mode 3 from  $0^{\circ}$  to EA and from CA3 to CA4. For the branches with complex eigenvalues (e.g., modes 4 and 5 and partially modes 2 and 3), the corresponding modes are in symmetry-broken phases. The spontaneous symmetry breaking occurs in reflected modes as well. Between the two CAs, the reflected mode 2 has imaginary  $k_2$  and displacement mode shapes that violate Eq. (11). For all the branches with broken modal symmetry, their averaged energy fluxes at the interface will be zero.

For the *m*th mode, its energy flux at the interface can be calculated as

$$F_2^{(m)}(x_1) = \int_{-h/2}^{h/2} -\frac{1}{2} \Re \left[ \bar{\sigma}_{2j}^{(m)}(x_1) \cdot (\partial_t \bar{u}_j^{(m)}(x_1))^* \right] \mathrm{d}x_1, \tag{12}$$

where the summation is done over  $j \in \{1, 2\}$ , and superscript \* denotes complex conjugate. The flux represents the time-averaged stress wave intensity in  $x_2$  direction. Figures 6(a) and 6(b) show the fluxes of the homogeneous medium modes and the phononic crystal modes, related to the bands in Fig. 3. Each mode shape used for this plot is normalized so that  $||[\bar{\mathbf{u}}_1^{(m)}, \bar{\mathbf{u}}_2^{(m)}]^\top|| = 1$ . In comparison with Fig. 3, one finds that an eigenvalue branch with complex-valued  $k_2$  (see Fig. 3) will have zero flux at the homogeneous-phononic interface, e.g., reflected mode 2 between CA1 and CA2 in Fig. 6(a) and transmitted mode 2 between 0° and CA3 in Fig. 6(b). This is expected since the modes with complex  $k_2$ are evanescent in  $x_2$  and only propagate along the surface  $(x_1 \text{ interface})$ . For the modes that possess branch points, the first order derivatives of their fluxes with respect to  $\theta$ become discontinuous at the special angles CAs and the EA. Therefore, these modes (mode 2 of the homogeneous medium, modes 2 and 3 of the phononic) undergo phase transitions at the CAs and the EA. On the other hand, a branch with real-valued  $k_1$  is capable of transporting energy in  $x_2$ , and its flux is non-zero. The branches with zero net flux are exactly the ones in the symmetry-broken phase.

The breaking of symmetry affects the particle motion trajectories as well. In time domain, the shape of the particle deformation given by  $\Re[u_1(x_1,t),u_2(x_1,t)]$  is in general an ellipse or a circle. A special case occurs when  $|\angle u_1 - \angle u_2| \in \{0,\pi\}$ , and the motion will be polarized as a straight line. Furthermore, the handedness of the trajectory is determined by the phase difference between  $u_1$  and  $u_2$ .



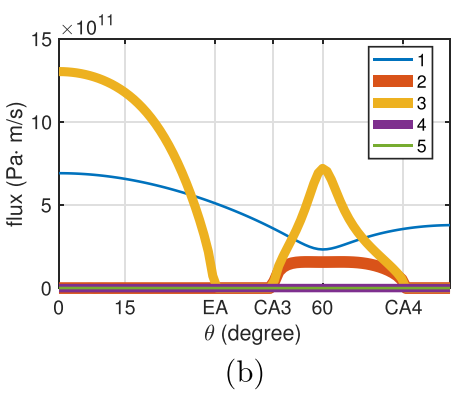


FIG. 6. (Color online) Time and unit cell averaged modal fluxes in  $x_2$  direction: (a) modes of the homogeneous medium and (b) modes of the phononic crystal.

The particle moves clockwise in time if  $\angle (u_1/u_2) < 0$ . The handedness becomes counterclockwise if  $\angle (u_1/u_2) > 0$ . Based on the periodicity  $\angle (u_1/u_2)(x_1) = \angle (u_1/u_2)(x_1+h)$  and the parity symmetry Eq. (11), it can be seen that, only when  $k_2$  is purely real, the motions at cell inversion centers  $x_1 = 0, \pm h/2$  will be polarized as lines, and the motions at  $x_1$  and  $-x_1$  must have reversed handedness. Three examples are shown in Fig. 7. The particle trajectories are plotted for five points uniformly sampled along  $x_1$ . The lack of symmetry for complex  $k_2$  is evident here. Even for a purely imaginary  $k_2$ , the behavior is distinct from that of a purely real  $k_2$ .

To summarize, the CAs and the EPs are identified as the spectral branch points between the complex and real eigenvalue branches. As the incident angle passes across these limits (CAs and EAs), certain eigen-mode(s) will switch between propagating ones and evanescent ones. A propagating mode carries energy in  $x_2$ , while an evanescent one only propagates along the  $x_1$  interface. At the branch points, spontaneous symmetry breaking occurs in the corresponding mode shapes. The modal energy fluxes will vanish in the symmetry-broken phases. The geometry and handedness of the motion trajectories are highly dependent on the

 $k_2$  eigenvalues as well. The types of  $k_2$  eigenvalues of the phononic modes are summarized in Fig. 8. The angle-dependent modal behaviors, summarized in Table I, will cause qualitative changes on the scattering signal and will be used as the base of the proposed sensing application.

#### **III. SOURCE LOCALIZATION**

Section II presents the eigen-analysis of the phononic medium and shows that the mode shapes vary drastically for different angles of incidence due to the existence of the branch points. In this section, we examine the oblique scattering responses and propose a deep-learning approach for source localization, based on the understanding of modal properties and their influences on the measured signals.

# A. Scattering responses

In a scattering configuration (with far-field assumption), the displacement and stress fields may be written as weighted summations of all the potential mode shapes (the lowest orders of which are shown in Sec. II). On the

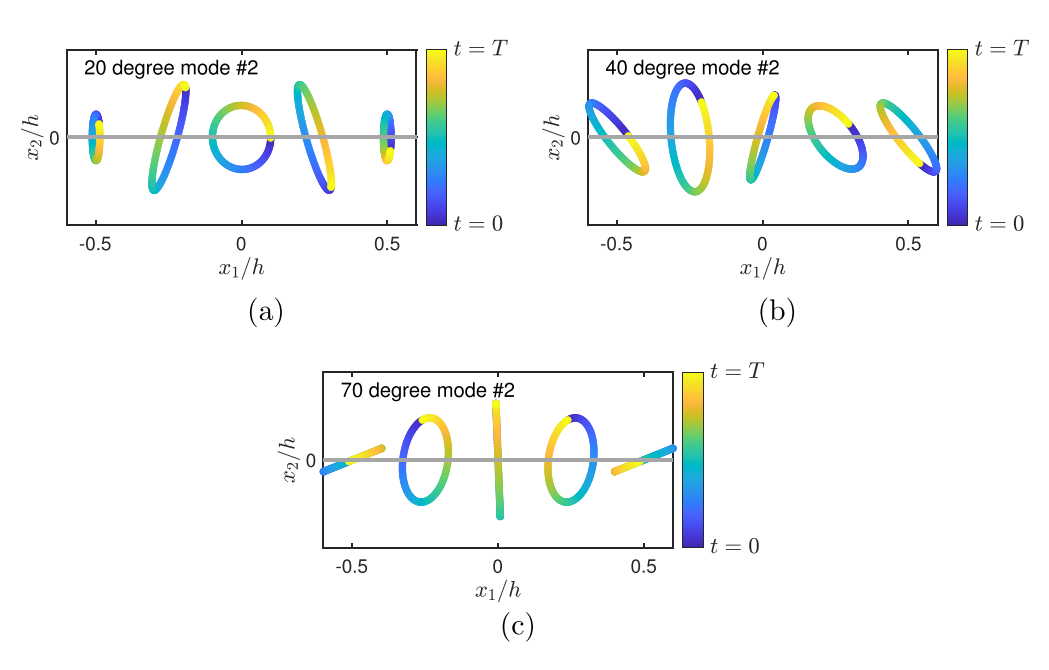


FIG. 7. (Color online) Examples of particle trajectories. (a) Case of imaginary  $k_2$ ; (b) case of complex  $k_2$ ; (c) case of real  $k_2$ .

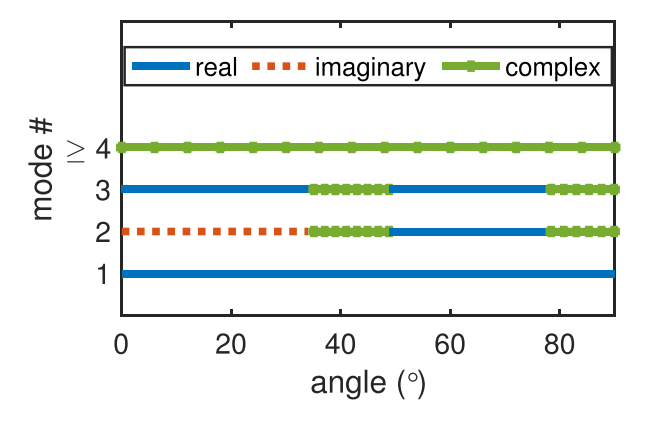


FIG. 8. (Color online) Summary of  $k_2$  eigenvalue types for the phononic eigen-modes.

transmission side of the interface (phononic domain) where the measurements are generally made, the field quantities are

$$u_{1,2}(\theta, x_1, x_2) = \sum_n T^{(n)} \bar{u}_{1,2}^{(n)} \exp\left[i(k_1(\theta)x_1 + k_2^{(n)}x_2)\right],$$
  

$$\sigma_{ij}(\theta, x_1, x_2) = \sum_n T^{(n)} \bar{\sigma}_{ij}^{(n)} \exp\left[i(k_1(\theta)x_1 + k_2^{(n)}x_2)\right],$$
(13)

where  $T^{(n)}$  is the coefficient of the *n*th transmitted mode and can be determined in a number of ways, including one based on Betti–Rayleigh reciprocity.<sup>27</sup>

The response of the phononic array, as described in Eq. (13), is first computed and then compared to that of a homogeneous medium to understand and highlight the effects of the micro-structures. For this comparison, the operating frequency and the incident/reflected domain material remain the same. The transmitted homogeneous domain has the following material properties: Lamé constants  $\lambda = 51.1\,\mathrm{GPa}$ ,  $\mu = 26.3\,\mathrm{GPa}$ , and density  $\rho = 7800\,\mathrm{kg/m^3}$ . The calculation of the solution follows standard analytical techniques, which are omitted here. To assess the angular sensitivity, the Euclidean distance is computed between signals from adjacent angles,

$$D(\theta) = ||\mathbf{s}(\theta) - \mathbf{s}(\theta + \delta\theta)||_{2}. \tag{14}$$

Here,  $\delta\theta=1^{\circ}$  is used, and a different value can also be used depending on the angular resolution of interest. The

TABLE I. Modal properties for different types of  $k_2$  eigenvalues.

| $k_2$                          | Real           | Imaginary | Complex    |
|--------------------------------|----------------|-----------|------------|
| Eigen-mode symmetry            | Unbroken       | Broken    | Broken     |
| Flux                           | Non-zero       | Zero      | Zero       |
| Trajectory at inversion center | Line           | Ellipse   | Ellipse    |
| Geometry <sup>a</sup>          | Anti-symmetric | Symmetric | Asymmetric |
| Chirality <sup>b</sup>         | Anti-symmetric | Symmetric | Asymmetric |

<sup>&</sup>lt;sup>a</sup>The shapes of the trajectories with respect to repeating unit cell (RUC) inversion center.

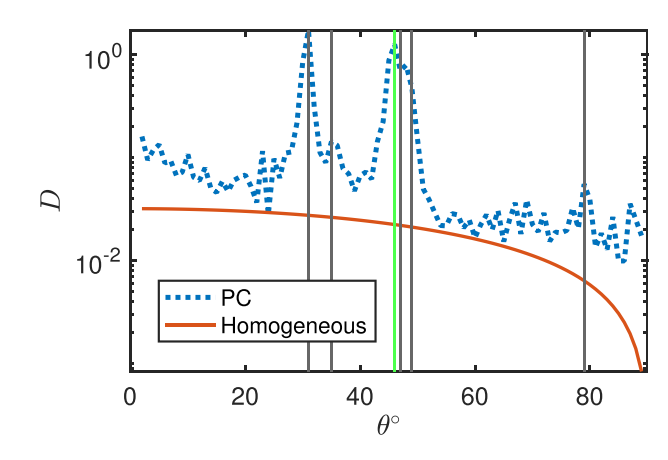


FIG. 9. (Color online) Signal distance comparison between PC and homogeneous systems. Higher values for the PC case imply more distinguishable angular responses over the adjacent angles.

response s is the measured  $\sigma_{11}$  quantity along one unit cell interface at the presumed sensor locations and is consistently normalized. Such distances are shown in Fig. 9 for both the PC and homogeneous system cases.

For the homogeneous medium, the eigen-modes and inherent scattering responses along the measurement interface always manifest as sinusoidal waves, regardless of the nature of the energy carried by the wave. This is because of the absence of micro-structural features in the medium. As a result, both eigen-modes appear identical along the measurement interface after amplitude normalization. Signal distances of consistently lower values are observed for the homogeneous medium, indicating greater similarity between  $s(\theta)$  and  $s(\theta+1)$ , particularly when the incident angle approaches  $90^{\circ}$ . This suggests that sensing systems with a homogeneous medium as the backbone material may be more susceptible to errors and noise.

In contrast, higher values of  $D(\theta)$  are observed for the phononic system, with several peaks at specific angles (CAs and EA, marked by black vertical lines), indicating increased sensitivity to angles. An additional peak near  $46^{\circ}$  is marked by a green vertical line, which corresponds to an anti-resonance behavior that has previously been reported<sup>27</sup> and explained.<sup>30</sup>

Owing to the rich modal behaviors of the PC system, the signals of the phononic medium show stronger angle dependency, and a larger variation in the adjacent response signals is observed. The enhanced sensitivity, especially near the special angles, allows for better differentiation of the scattering responses from different angles of incidence, creating promising potential for source localization applications.

# B. Angle classification

The proposed source localization strategy leverages the knowledge of feature-rich modal behaviors and is stated as follows. The localization approach first seeks advantages from the existence of branch points (EP and CA). As the participating eigen-modes undergo symmetry breaking at

<sup>&</sup>lt;sup>b</sup>The handedness directions of the trajectories with respect to RUC inversion center

the exact angles associated with the branch points, the measurable responses exhibit qualitative changes in addition to the quantitative increase/decrease in the amplitudes. It is observed through the signal distance comparison (Fig. 9) that local peaks exist at these special angles, which indicate relatively distinct response behaviors across these angles.

While the presence of EP/CA only promotes the sensitivity at the certain relevant angles, the phononic response at other angles still possesses micro-structural features (i.e., unlike simply sinusoidal waves in the homogeneous case). These micro-structural features provide angle-dependent information within each unit cell through previously determined eigen-modes. From the linear algebra point of view, the scattered field is expected to lie in the subspace  $M(\theta)$  spanned by the first few dominant modes. Assuming that  $n_p$  measurements are taken per unit cell along the interface, and  $n_c$  cells are used, we have

$$\mathbf{s}(\theta) \in M(\theta) = \operatorname{span}\{\mathbf{m}^{(1)}(\theta), \mathbf{m}^{(2)}(\theta), \mathbf{m}^{(3)}(\theta)\} \subset \mathbb{C}^{n_p n_c},$$
(15)

where **s** is the frequency domain complex amplitudes measured at the sensors with length  $n_p n_c$ , and  $\mathbf{m}^{(n)}$  is the *n*th mode shape vector (stress or displacement quantities) of the same length sampled at the same locations.

With the modal features showing sensitive angular dependence, especially in their symmetry properties, both the scattered field and the underlying subspace  $M(\theta)$  will inherently possess high variance with respect to the angles. For any complex vector  ${\bf s}$  taken from measurement, if it is identified as an element of subspace  $M(\theta)$ , then the incident angle is  $\theta$ . This method takes advantage of the fact that the subspace spanned by the dominant eigen-modes is sensitive to incident angles. Therefore, a suitable data processing method is needed to highlight and identify such information. To implement localization, artificial neural networks (ANNs) can be used to learn and extract the abstract features of the subspace  $M(\theta)$  based on the modal knowledge.

In the following, an example of source localization is shown using a feed-forward deep neural network (DNN) setup. Notice that other NN architectures, such as convolutional NNs, can also be used for this purpose. In brief, the NN is trained using randomly weighted and summed mode shapes that span the response subspace and contain the angle-sensitive features for the NN to learn. The data processing procedures and the detailed implementation of the NN are presented in Appendix A. The quantity selected for measurement in this example is the normal stress component  $\sigma_{11}$ . For practical measurement considerations, one can use surface mount pressure sensors or optical methods, such as interferometry, to collect the response signals. Alternatively (and perhaps more suitably in practice), one can also employ piezoelectric materials in the micro-structured sensor design, which will convert stress into electric signals.

With the NN trained and converged, the test set, which consists of the scattering signals from 1° to 89° (calculated in this case based on the Betti-Rayleigh reciprocity

principle<sup>27</sup>), is then fed into the NN to verify the sensing performance. The signals used here are slightly corrupted with additive white Gaussian noises added to the frequency domain complex amplitude. The signal-to-noise ratio (SNR) is 25 dB. The localization performance of the trained NN is compared with that of a conventional method, DAS, which is applied to the same phononic response data. A simplified DAS algorithm is used here and is shown in Appendix B. Detailed studies of DAS can be found in the literature. 31,32 Figure 10 shows the performance comparison between DAS and DNN. While the branch points and mode shapes are present for the same system, the DAS method does not benefit from these micro-structural features. This is because the DAS approach relies on the Fourier transform, which focuses on the signal periodicity and is not designed to pick up the micro-structural features. The DAS [Fig. 10(a)] produces wider main lobes and has higher side lobes. On the contrary, the DNN approach takes advantage of the modal information and produces [Fig. 10(b)] sharp peaks at the predicted angles. The sidelobe levels are significantly suppressed. The DNN also leads to higher precision (93.26%) in identifying incident angles compared to the DAS (84.27%). A detailed example can be seen in Fig. 10(c), where the DNN outperforms the DAS and leads to the correct angle of incidence. However, the trained DNN is not fully error-free either. In Fig. 10(d), for instance, the DNN mistakenly predicts the 88° angle to be 87°. The end-fire sources present challenges for any AoA estimation algorithm. Improved performance may be achievable by adjusting the NN architecture and fine tuning the hyperparameters or, more fundamentally, by design of microstructure for higher modal sensitivity at such angles of incidence. In general, the proposed approach using the NN to identify angle of incidence shows strong potential and benefits in the localization application. By incorporating microstructural features and utilizing the eigen-mode physics, this approach adds extra strength and can be implemented as a parallel procedure to the existing ML-based approaches.

# **IV. CONCLUSION**

In this work, we exploit the eigen-wavevector band structure of micro-structured media under oblique scattering and present the sensing potentials of the micro-structural responses based on deep learning of the angle-dependent modal features. In the studied oblique stress wave scattering problem, the modal symmetry breaking at the CAs and the EPs is identified and discussed in detail through its modal shape symmetry, flux, and polarization. It is understood that the scattering signals lie predominantly in the subspace spanned by the lower eigen-modes, and this subspace has inherently strong dependence on the incident angle.

We use the angle-dependent eigen-modes as the training data to develop a ML approach for source localization. An ANN is trained with random sampling of the subspace spanned by the eigen-modes as the training input. The trained NN is able to identify the angle-dependent features

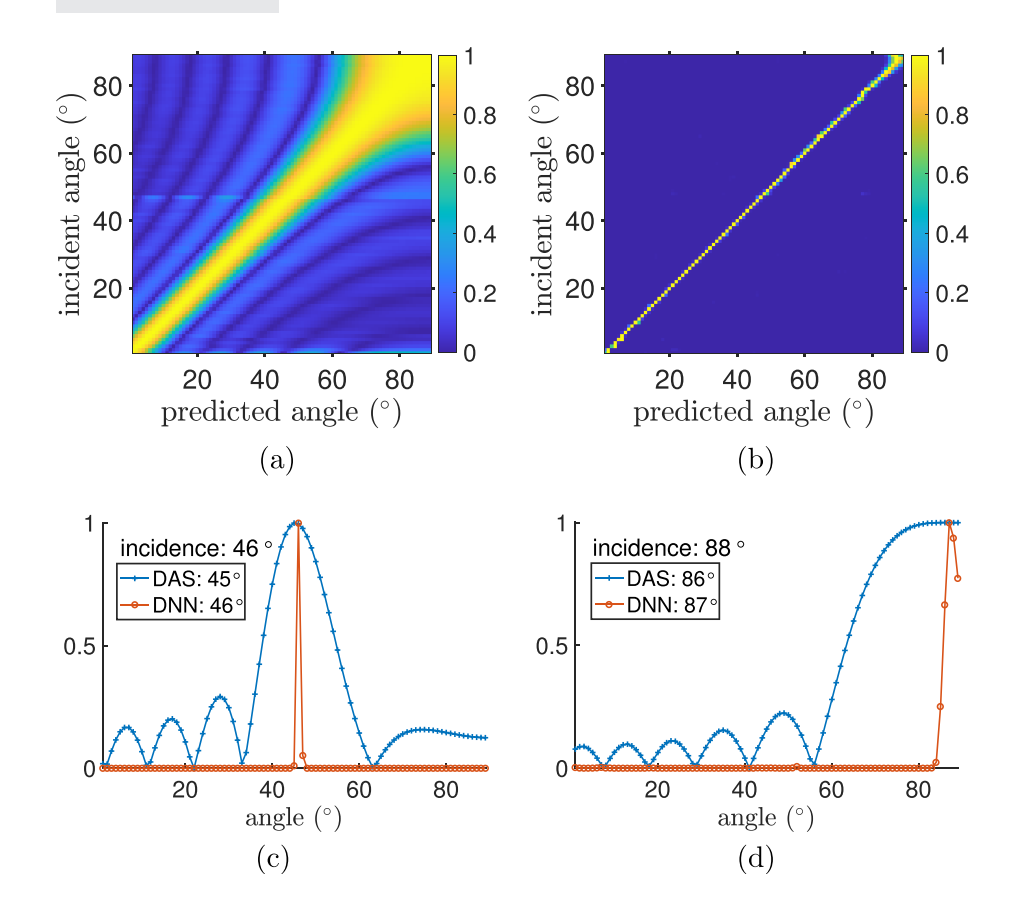


FIG. 10. (Color online) Localization outputs of DAS and DNN algorithms applied to the same collected data set and sensors. To compare between two methods, all the outputs are re-scaled from 0 to 1 and are shown in the linear scale. (a) DAS, 84.27% accuracy; (b) DNN, 93.26% accuracy; (c) 46° incidence; (d) 88° incidence.

of the modal subspace and shows major improvements in identifying the angle of incidence based on scattering as input test data in comparison with the standard DAS approach, in terms of sidelobe size and main lobewidth. Such an approach can be applied to localization problems with a generic sensor domain whose 2D eigen-modes are pre-extracted for ML.

The scope of this paper is limited to computational investigation, and the example shown is a theoretical proof of concept. Of practical importance is the evaluation of imperfection effects, such as potential defects in the periodicity, their influences on the EPs, and the resulting error bounds. However, as existing computational methods require perfect periodicity in the boundary condition, we suggest that such an uncertainty analysis should be the subject of a future study.

To summarize, the proposed method

- highlights and utilizes the physics of the band structure and eigen-modes for sensing purposes;
- shows that ANNs can be trained using eigen-modes in order to identify incident angles;
- can be continuously improved with the fast-growing deep-learning techniques; and
- can be optimized through careful micro-structural design, leading to feature-rich and wavevector-sensitive modal subspaces.

While the developed NN shows relatively successful identification of each angle of incidence, such an approach essentially relies on the fact that the signals are composed of known modal components. Therefore, the sensing robustness is subject to variation in the modal response, although the accuracy can be numerically optimized through the training process. To develop a more physically robust approach, we suggest further leveraging the topological features in the band structure and mode shapes and effectively amplifying the switching in energy and symmetry of certain modes at the branch points. To this end, one might seek to develop kernels that highlight the mode-switching behaviors near CAs and EPs by differentiating the expected scattering response at neighboring angles. From the design perspective, two approaches can be considered to increase the angular sensitivity over many angles of interest. The first method would be to seek micro-structural designs with tailored geometrical or material features, so that the band structure exhibits a relatively large number of branch points. These branch points would create finer regions in the angular space, and between different angle regions the response would be inherently different. The second approach is to manifest only one branch point instead of many and focus on the response variation across this particular angle. By rotating the sensor array and simultaneously evaluating the collected data, abrupt changes will be observed whenever the incoming angles align with the branch point angle, thus, providing the angle(s) of arrival with high accuracy.

#### **ACKNOWLEDGMENTS**

The authors acknowledge National Science Foundation support for this work through Grant No. 1825969 to

University of Massachusetts, Lowell, and Grant No. 1825354 to Illinois Institute of Technology, Chicago.

#### APPENDIX A: NN IMPLEMENTATION

### 1. Data preprocessing

In the example here,  $n_p = 6$  measurements are taken per unit cell, and  $n_c = 10$  cells are used in total. The data collection points are measured along the interface  $x_2 = 0$  with a uniform spacing of h/6. Such a sensor array is referred to as a uniform linear array (ULA).

The input to the NN will represent complex vectors in  $M(\theta)$  in the training stage, and the output will indicate the angle  $\theta$ . For each incident angle  $\theta$ , 2100 training samples are prepared and labelled by the associated integer angle  $\theta \in [1^{\circ}, 89^{\circ}]$ . Each training sample is given by

$$\mathbf{t}(\theta) = c^{(1)}\mathbf{m}^{(1)}(\theta) + c^{(2)}\mathbf{m}^{(2)}(\theta) + c^{(3)}\mathbf{m}^{(3)}(\theta).$$
 (A1)

Here,  $\mathbf{m}^{(n)}(\theta)$  is the nth  $\sigma_{11}$  mode shape vector of length  $n_p n_c$  associated with incident angle  $\theta$ , and it includes the  $ik_1(\theta)x_1$  phase. The complex coefficient  $c^{(n)}$  of each mode is randomly selected in such a way that both  $\Re c^{(n)}$  and  $\Im c^{(n)}$  have uniform distributions between -0.5 and 0.5. A validation set is prepared in the same fashion and consists of 450 labelled samples  $\mathbf{v}(\theta)$  for each value of  $\theta$ . Unlike the training and validation sets, the test set consists of the scattering signals  $\mathbf{s}$  instead of random vectors in  $M(\theta)$ . It should be highlighted that the test set is unknown to the NN and will, therefore, provide the evaluation of the sensing performance.

It is necessary to normalize input data properly to render it independent of source strength. The complex vectors  $\mathbf{b} = \mathbf{t}$ ,  $\mathbf{v}$ , or  $\mathbf{s}$  are normalized so that

$$||\mathbf{b}|| = 1. \tag{A2}$$

Then the complex vectors  $\mathbf{b} = \mathbf{t}$ ,  $\mathbf{v}$ , or  $\mathbf{s}$  are converted into real-valued arrays  $\mathbf{b}'$  before feeding into the NN,

$$\mathbf{b}' = \begin{pmatrix} |\mathbf{b}| \\ \cos \angle \mathbf{b} \\ \sin \angle \mathbf{b} \end{pmatrix} \in \mathbb{R}^{3n_p n_c}. \tag{A3}$$

The amplitude and angle operators are applied to each component of vector **b** separately. The redundancy of applying the sin and cos operators separately is intentional.

# 2. NN

In this example, a feed-forward NN is used for deep learning of the eigen-modes and for classifying the incident angle of unknown signals. The NN architecture is shown in Fig. 11. It includes an input layer with 180 neurons for  $n_p = 6$  and  $n_c = 10$ . The NN parameters, such as layer and node number, are determined using a hyper-parameter search, as proposed in the literature.<sup>26</sup> The input array is formatted based on Eq. (A3). The output layer has 89 neurons,

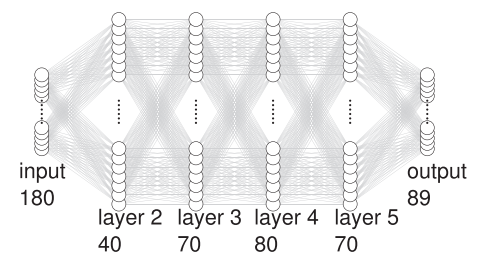


FIG. 11. The feed-forward (fully connected) NN architecture. The numbers of neurons (excluding the bias unit) are labelled under the layers. The bias units of the first five layers are not shown.

with each representing an integer angle  $\in [1^{\circ}, 89^{\circ}]$  through one-hot encoding. The angle labels of the training and validation samples are represented by binary vectors of length 89. It is also possible to use a single continuous output as the predicted angle. However, the discretized output layer is used here for future extension of multi-source applications.

At the hidden layers (2–5), the NN operation is as follows. Let  $s_j$  denote the number of neurons (bias unit not included) of the jth layer. The neuron values at the jth layer can be written as a column vector  $\mathbf{a}^{(j)}$ . The vector  $\mathbf{a}^{(j)}$  has a length of  $s_j + 1$  to include the bias unit (for  $j \leq 5$ ). For example, the training input is  $\mathbf{a}^{(1)} = [1, \mathbf{t}']^{\top}$ , and  $\mathbf{t}'$  is a real vector of length 180. The value of each neuron is obtained by first computing a weighted sum of all neurons (with the bias unit) in the previous layer. This can be written as a matrix calculation,

$$\mathbf{z}^{(j)} = \mathbf{\Theta}^{(j-1)} \mathbf{a}^{(j-1)},\tag{A4}$$

where  $\Theta^{(j-1)}$  is an  $s_j$  by  $s_{j-1}+1$  real matrix representing the connection weights between layer j-1 and layer j. Then the batch normalizing transform is applied to the updated vector  $\mathbf{z}^{(j)}$  to obtain  $\bar{\mathbf{z}}^{(j)}$ . The batch normalization effectively recenters and re-scales the data array to achieve faster and more stable performance of the NN.<sup>33</sup> This is followed by a non-linear activation using the rectified linear unit (ReLU) function,

$$ReLU(x) = \max(0, x). \tag{A5}$$

The ReLU activation is widely chosen for NNs due to its multiple advantages,<sup>34</sup> such as better gradient propagation and computational efficiency. Finally, the updated state of the layer is given by

$$\mathbf{a}^{(j)} = \text{ReLU}(\bar{\mathbf{z}}^{(j)}). \tag{A6}$$

For the output layer, we have

$$\mathbf{z}^{(6)} = \boldsymbol{\Theta}^{(5)} \mathbf{a}^{(5)}. \tag{A7}$$

The final output is activated through the sigmoid function,

$$\mathbf{a}^{(6)} = S(\mathbf{z}^{(6)}) = \frac{1}{1 + \exp(-\mathbf{z}^{(6)})}.$$
 (A8)

The sigmoid function, for each output neuron, returns a value in the range 0–1. The output  $\mathbf{h} = \mathbf{a}^{(6)}$  predicts the probability of each angle.

The NN is first randomly initialized. In the training process, the training set (2100 samples per angle) is randomly separated into 25 mini-batches and fed into the NN for 100 epochs. At each training iteration, one batch of training data is passed through the NN. A cross-entropy cost function<sup>35</sup> is then evaluated as

$$J(\mathbf{P}) = -\frac{1}{N} \sum_{n=1}^{N} \sum_{i=1}^{K} (T_{i,n} \log (h_{i,n}) + (1 - T_{i,n}) \log (1 - h_{i,n})),$$
(A9)

where N = 2100 \* 89/25 and K = 89 are the numbers of samples and incident angles, respectively. The target value of the *i*th output neuron for the *n*th sample is  $T_{i,n} \in \{0,1\}$ . The output value of the *i*th neuron for the *n*th sample is  $h_{i,n} \in [0,1]$ . Here, the vectorized variable **P** contains all the NN parameters to be optimized, including the connection weights  $\Theta$ , the offset factors, and the re-scale factors. At the end of each iteration, the cost J and its gradients with respect to **P** are evaluated. Then the parameters **P** are updated based on gradient descent and will be used for the next iteration. The training process aims to minimize the cost and find the best set of NN parameters. Figure 12 shows the convergence of the training accuracy for each iteration.

The final training accuracy for the last batch is 93.93%. Then the NN is tested using a validation set that has 450 labelled samples per angle. The validation set is a secondary set of data that is not learned by the NN and can, therefore, provide an unbiased evaluation of the NN fitness. In this case, the accuracy for the validation set is 93.96%. Recall that all the samples in the training set and the validation set are made up by randomly weighted eigen-modes. The relatively good accuracy achieved on these eigen-modes indicates that the subspace spanned by the eigen-modes indeed has angle-sensitive features that can be learned by the NN.

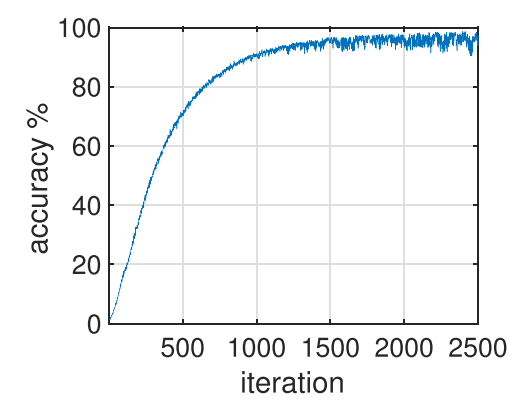


FIG. 12. (Color online) The convergence plot shows the training accuracy for each iteration (mini-batch).

#### **APPENDIX B: DAS**

DAS is one of the fundamental source localization algorithms. It utilizes the spatial discrete Fourier transform to identify the dominant wavevector components/the incident angle. The DAS output for a given signal  $\mathbf{s}$  is

$$y(\phi) = \mathbf{w}^*(\phi)(\mathbf{s} + \mathbf{n}),\tag{B1}$$

where  $y(\phi)$  is the beamformer output for trial angle  $\phi$ , \* denotes complex conjugate, the signal s is a column vector associated with an unknown angle, and **n** is the additive noise. The weight array is

$$\mathbf{w}(\phi) = (1 \quad \exp(ik_{in}d\sin\phi) \quad \exp(2ik_{in}d\sin\phi) \\ \cdots \quad \exp(i(n_pn_c - 1)k_{in}d\sin\phi)), \tag{B2}$$

where  $k_{in}$  is the incident wavevector, d is the sensor distance, and  $n_p n_c$  is the total number of sensors. The trial angle  $\phi$  that maximizes y is the evaluated angle of incidence.

<sup>1</sup>P. Chiariotti, M. Martarelli, and P. Castellini, "Acoustic beamforming for noise source localization—Reviews, methodology and applications," Mech. Syst. Signal Process. **120**, 422–448 (2019).

<sup>2</sup>D. Joffre, C. Niezrecki, and P. Avitabile, "Array directivity enhancement by leveraging angle-dependent scattering," J. Acoust. Soc. Am. **147**(3), 1673–1680 (2020).

<sup>3</sup>S. Nemat-Nasser, H. Sadeghi, A. Amirkhizi, and A. Srivastava, "Phononic layered composites for stress-wave attenuation," Mech. Res. Commun. 68, 65–69 (2015).

<sup>4</sup>F. Aghighi, J. Morris, and A. V. Amirkhizi, "Low-frequency microstructured mechanical metamaterials," Mech. Mater. **130**, 65–75 (2019).

<sup>5</sup>L. D'Alessandro, R. Ardito, F. Braghin, and A. Corigliano, "Low frequency 3D ultra-wide vibration attenuation via elastic metamaterial," Sci. Rep. **9**(1), 8039 (2019).

<sup>6</sup>W. Elmadih, D. Chronopoulos, and J. Zhu, "Metamaterials for simultaneous acoustic and elastic bandgaps," Sci. Rep. **11**(1), 14635 (2021).

<sup>7</sup>J. Morris, W. Wang, D. Shah, T. Plaisted, C. J. Hansen, and A. V. Amirkhizi, "Expanding the design space and optimizing stop bands for mechanical metamaterials," Mater. Des. 216, 110510 (2022).

<sup>8</sup>Y. Guo, T. Dekorsy, and M. Hettich, "Topological guiding of elastic waves in phononic metamaterials based on 2D pentamode structures," Sci. Rep. 7(1), 18043 (2017).

<sup>9</sup>A. V. Amirkhizi and V. Alizadeh, "Overall constitutive description of symmetric layered media based on scattering of oblique SH waves," Wave Motion 83, 214–226 (2018).

<sup>10</sup>R. Adlakha, M. Moghaddaszadeh, M. A. Attarzadeh, A. Aref, and M. Nouh, "Frequency selective wave beaming in nonreciprocal acoustic phased arrays," Sci. Rep. 10(1), 21339 (2020).

<sup>11</sup>W. D. Heiss, "Exceptional points of non-Hermitian operators," J. Phys. A: Math. Gen. 37(6), 2455–2464 (2004).

<sup>12</sup>G. Shmuel and N. Moiseyev, "Linking scalar elastodynamics and non-Hermitian quantum mechanics," Phys. Rev. Appl. 13(2), 024074 (2020).

<sup>13</sup>W. Wang and A. V. Amirkhizi, "Exceptional points and scattering of discrete mechanical metamaterials," Eur. Phys. J. Plus 137(4), 414 (2022).

<sup>14</sup>A. V. Amirkhizi and W. Wang, "Reduced order derivation of the twodimensional band structure of a mixed-mode resonator array," J. Appl. Phys. 124(24), 245103 (2018).

<sup>15</sup>J. Wiersig, "Enhancing the sensitivity of frequency and energy splitting detection by using exceptional points: Application to microcavity sensors for single-particle detection," Phys. Rev. Lett. 112(20), 203901 (2014).

<sup>16</sup>J. Wiersig, "Sensors operating at exceptional points: General theory," Phys. Rev. A 93(3), 033809 (2016).

<sup>17</sup>P. Djorwe, Y. Pennec, and B. Djafari-Rouhani, "Exceptional point enhances sensitivity of optomechanical mass sensors," Phys. Rev. Appl. 12(2), 024002 (2019).

# https://doi.org/10.1121/10.0022325

JASA

- <sup>18</sup>X. Zhu, H. Ramezani, C. Shi, J. Zhu, and X. Zhang, "PT-symmetric acoustics," Phys. Rev. X 4(3), 031042 (2014).
- <sup>19</sup>A. A. Mokhtari, Y. Lu, and A. Srivastava, "On the properties of phononic eigenvalue problems," J. Mech. Phys. Solids 131, 167–179 (2019).
- <sup>20</sup>A. Srivastava and J. R. Willis, "Evanescent wave boundary layers in metamaterials and sidestepping them through a variational approach," Proc. R. Soc. A 473(2200), 20160765 (2017).
- <sup>21</sup>S. I. Rokhlin and W. Wang, "Critical angle measurement of elastic constants in composite material," J. Acoust. Soc. Am. 86(5), 1876–1882 (1989).
- <sup>22</sup>D. A. Abraham, Underwater Acoustic Signal Processing, Modern Acoustics and Signal Processing (Springer, Cham, Switzerland, 2019), pp. 3–32.
- <sup>23</sup>B. Lustig, G. Elbaz, A. Muhafra, and G. Shmuel, "Anomalous energy transport in laminates with exceptional points," J. Mech. Phys. Solids 133, 103719 (2019).
- <sup>24</sup>H. Niu, E. Reeves, and P. Gerstoft, "Source localization in an ocean waveguide using supervised machine learning," J. Acoust. Soc. Am. 142(3), 1176–1188 (2017).
- <sup>25</sup>H. Niu, E. Ozanich, and P. Gerstoft, "Ship localization in Santa Barbara Channel using machine learning classifiers," J. Acoust. Soc. Am. 142(5), EL455–EL460 (2017).
- <sup>26</sup>E. Ozanich, P. Gerstoft, and H. Niu, "A feedforward neural network for direction-of-arrival estimation," J. Acoust. Soc. Am. 147(3), 2035–2048 (2020).

- <sup>27</sup>A. A. Mokhtari, Y. Lu, Q. Zhou, A. V. Amirkhizi, and A. Srivastava, "Scattering of in-plane elastic waves at metamaterial interfaces," Int. J. Eng. Sci. 150, 103278 (2020).
- <sup>28</sup>W. Wang and A. V. Amirkhizi, "Reduced order modeling of dynamic mechanical metamaterials for analysis of infinite and finite systems," J. Appl. Mech. **90**(9), 091009 (2023).
- <sup>29</sup>J. Achenbach, "Plane harmonic waves in elastic half-spaces," in Wave Propagation in Elastic Solids (Elsevier, Amsterdam, 1975), pp. 165–201.
- <sup>30</sup>H. Khodavirdi, A. A. Mokhtari, and A. Srivastava, "Scattering of mechanical waves from the perspective of open systems," Mech. Mater. 172(February), 104399 (2022).
- <sup>31</sup>M. R. Bai, J.-G. Ih, and J. Benesty, Acoustic Array Systems (Wiley, Singapore, 2013).
- <sup>32</sup>V. Perrot, M. Polichetti, F. Varray, and D. Garcia, "So you think you can DAS? A viewpoint on delay-and-sum beamforming," Ultrasonics 111, 106309 (2021).
- <sup>33</sup>S. Ioffe and C. Szegedy, "Batch normalization: Accelerating deep network training by reducing internal covariate shift," in *Proceedings of the 32nd International Conference on Machine Learning (ICML 2015)*, Lille, France (July 6–11, 2015) (Microtome Publishing, Brookline, MA), Vol. 37, pp. 448–456.
- <sup>34</sup>X. Glorot, A. Bordes, and Y. Bengio, "Deep sparse rectifier neural networks," in *Proceedings of the 14th International Conference on Artificial Intelligence and Statistics (AISTATS)*, Fort Lauderdale, FL (April 11–13, 2011) (Microtome Publishing, Brookline, MA), pp. 315–323.
- <sup>35</sup>K. P. Murphy, Machine Learning: A Probabilistic Perspective (MIT, Cambridge, MA, 2012).